energies

MDPI

Article

Non-Invasive Detection of Lithium-Metal Battery Degradation

Pietro Iurilli [1,*], Luigi Luppi [1,2] and Claudio Brivio [2]

[1] Sustainable Energy Center, CSEM, 2002 Neuchâtel, Switzerland
[2] Department of Energy, Politecnico di Milano, 20156 Milano, Italy
* Correspondence: pietro.iurilli@csem.ch

Abstract: The application of Lithium Metal Batteries (LMBs) as secondary cells is still limited due to dendrite degradation mechanisms arising with cycling and responsible for safety risk and early cell failure. Studies to prevent and suppress dendritic growth using *state-of-the-art* materials are in continuous development. Specific detection techniques can be applied to verify the internal condition of new LMB chemistries through cycling tests. In this work, six non-invasive and BMS-triggerable detection techniques are investigated to anticipate LMB failures and to lay the basis for innovative self-healing mechanisms. The novel methodology is based on: (i) defining detection parameters to track the evolution of cell aging, (ii) defining a detection algorithm and applying it to cycling data, and (iii) validating the algorithm in its capability to detect failure. The proposed methodology is applied to Li||NMC pouch cells. The main outcomes of the work include the characterization results of the tested LMBs under different cycling conditions, the detection techniques performance evaluation, and a sensitivity analysis to identify the most performing parameter and its activation threshold.

Keywords: lithium metal batteries; dendrites; detection technique; self-healing

Citation: Iurilli, P.; Luppi, L.; Brivio, C. Non-Invasive Detection of Lithium-Metal Battery Degradation. *Energies* **2022**, *15*, 6904. https://doi.org/10.3390/en15196904

Academic Editors: Siamak Farhad and Carlos Miguel Costa

Received: 19 August 2022
Accepted: 7 September 2022
Published: 21 September 2022

1. Introduction

The continuous demand for electrical storage systems with ever-growing energy density has focused research and innovation on the development of batteries that can provide superior performance over the Lithium Ions Batteries (LIBs), also called beyond-LIB technologies [1–3]. A detailed review about cathode and anode materials for developing *state-of-the-art* and future battery technologies is given by Divakaran et al. in [4], highlighting the viable materials to be used for research and development of new LIBs. Among many beyond-LIBs, rechargeable Lithium Metal Batteries (LMBs) have been extensively researched in recent years for their valuable properties [5,6]. Lithium metal is an ideal anode material for its extremely high theoretical specific capacity (3860 mAh/g), low density (0.59 g/cm^3) and the lowest negative electrochemical potential (−3.05 V vs. standard hydrogen electrode). However, the applications of secondary LMBs have always been limited due to one main degradation mechanism: the dendrite growth leading to safety risk and early cell failure [7–10]. Whatever may be the testing conditions (e.g., current rate, voltage range, temperature), LMB degradation starts from the Beginning of Life (BoL) [11]. Dendrite nucleation takes place from the inhomogeneities of the Solid Electrolyte Interphase (SEI) which represents a high conductive pathway for lithium ions. The concentrated lithium ions are reduced causing fractures in the SEI layer due to volumetric expansion. These fractures represent suitable sites for deposition of lithium metal forming the dendrite [12,13]. The high conductivity of the initial deposition causes the dendritic structure to continuously grow assuming various morphologies which depend on cycling conditions [11,14]. In [15] Frenck et al. classified these morphologies in three main groups: (i) whiskers, which are long and thin needle-shaped lithium metal frames growing from the anode and covered with the SEI layer; (ii) mossy lithium, which corresponds to an accumulation of solid lithium cluster with holes and internal cavities filled with electrolyte and characterized by a large interface surface area that increases reactions with the electrolyte;

and (iii) fractal dendrites, which are thin, highly ramified structures growing directly from a layer of mossy lithium. The three listed morphologies occur in different testing conditions or after different timing that is always strictly correlated to the specific components and design of the cell under test [15]. Knowing the effects of these morphologies contribute to understanding LMB degradation. During the cell's early cycles, dendritic deposition is mossy and then progresses in a fractal configuration when the lithium ion concentration reaches zero value at the interface between the anode and the electrolyte [11,15]. The transition between mossy and fractal dendrites is described by Sand's principle and occurs at the so-called Sand's time [16]. This transition time depends on the applied current density and on the total amount of exchanged capacity. For instance, large current density leads to a fast-growing fractal dendrite structure that may penetrate the separator and may cause hazardous internal short circuits [17,18]. In addition to the short circuit risk, during the discharging phase, lithium metal is mainly stripped from dendrites causing the detachment of dendrite sections and resulting in electrically isolated inactive dead lithium [19,20]. Chen et al. deepened the dead lithium impact on the mass transport in LMBs, proving that the growth of a dead lithium layer, characterized by a small lithium ions diffusive coefficient, is associated with an increase of the electrode overpotential which results in an arcing effect of the voltage shape profile [21]. At later cycles, as the dead lithium layer thickens and the overpotential becomes more significant, the cell begins to be cycled between a much shallower voltage range, preventing a complete lithiation or delithiation of the cathode, thus resulting in cell capacity fade [22].

Studies to prevent and suppress the dendrite growth mechanisms are under continuous development and are classified as a self-healing method [23]. The most recent promising solutions involve the use of optimized electrolytes with protective additives, the modulation of lithium metal anodes and the introduction of piezoelectric separators [24–27]. Characterizing new LMB chemistries through the application of a detection technique becomes fundamental to study their behavior and to determine when dendritic degradation is going to occur in order to act accordingly. An extensive review about existing and emerging detection techniques for LMB degradation is given by Paul et al. in [28]. These detection techniques are classified into four groups, depending on their nature and application method: electrochemical in situ methods, mechanical methods, spectroscopic operando methods and chemical ex situ methods. Electrochemical in situ methods are the most promising for BMS application [29,30]. However, existing works on LMBs degradation detection are all at the development stage and have only investigated the possibility to track phenomena but not to concretely use that information to trigger actions [28].

This work analyzes and combines non-invasive detection techniques to present a novel methodology to detect LMBs degradation, laying the basis for the concreate application of LMBs self-healing mechanisms triggered by the BMS. The work is structured as follows. Section 2 shows the six selected electrochemical characterization techniques and the innovative methodology developed to apply the detection parameters as degradation identification tools. Section 3 presents the details of the experimental procedure, the most relevant results of the tests and the application of the detection techniques for the determination of approaching degradations. Section 4 discusses and identifies the most performing detection parameter based on an extensive sensitivity analysis.

2. Materials and Methods

This section includes an overview of non-invasive characterization techniques for the detection of degradation mechanisms in LMBs and the developed methodology to benchmark and validate the detection parameters extracted by the characterization techniques. The methodology has been applied to lithium metal pouch cells produced in the framework of the Horizon 2020 project HIDDEN [31]. The cells consist of Lithium Nickel Manganese Cobalt Oxide ($LiNi_{0.5}Mn_{0.3}Co_{0.2}O_2$) as the active cathode, coated on top of a 15 µm thick aluminum current collector, and a copper foil double coated with lithium metal mixed with a small amount of aluminum as an anode material (99.7% Li and 0.3% Al) and a monolayer

polypropylene separator of 20–40 µm thickness. Commercially available *state-of-the-art* electrolyte for lithium metal anodes is added. A total of 5 cathode foils and 6 anode foils alternated with 12 separator layers are stacked into the pouch cell. The stack is prepared under a control environment in a glovebox and filled with the electrolyte before sealing in a four-layer pouch foil of PET, oriented nylon, aluminum and polypropylene housing. The cells have been produced in three batches at different times, with an average weight of 11 g, a theoretical capacity of 670 mAh and an estimated gravimetric energy density of 225 Wh/Kg.

2.1. Detection Techniques

As mentioned in the introduction, electrochemical non-invasive techniques that do not require cell modifications or major add-ons in a system are selected here for possible application in real BMS. Aging tracking methods, already verified for LIBs, are analyzed to select the most relevant techniques for the application with LMBs.

Incremental capacity (IC) is used as an effective method to analyze the aging mechanisms based on the discrete derivative of the cell's voltage with respect to the exchanged capacity dQ/dV [32–35]. Voltage plateaus during charging and discharging processes, corresponding to specific electrochemical phase transitions, are converted into clearly identifiable peaks on the IC curve as shown in Figure 1a. Several works proved that Loss of Active Anode Material (LAM), responsible for capacity fade and limited cyclability, leads to peak intensity reduction and peak position variation in the dQ/dV curve [36–40]. Since the formation of dead lithium causes detachment and isolation of active lithium metal, its development is directly detectable on the IC profile. Similarly to IC, *Differential Voltage* (DV) analysis is an investigation technique given by the inverse derivative dV/dQ [41–43]. Therefore, the DV curve provides information similar to the IC curve but with a different representation (peaks of IC are valleys of DV). Depending on the specific application, it may be more appropriate to use the IC or the DV profile.

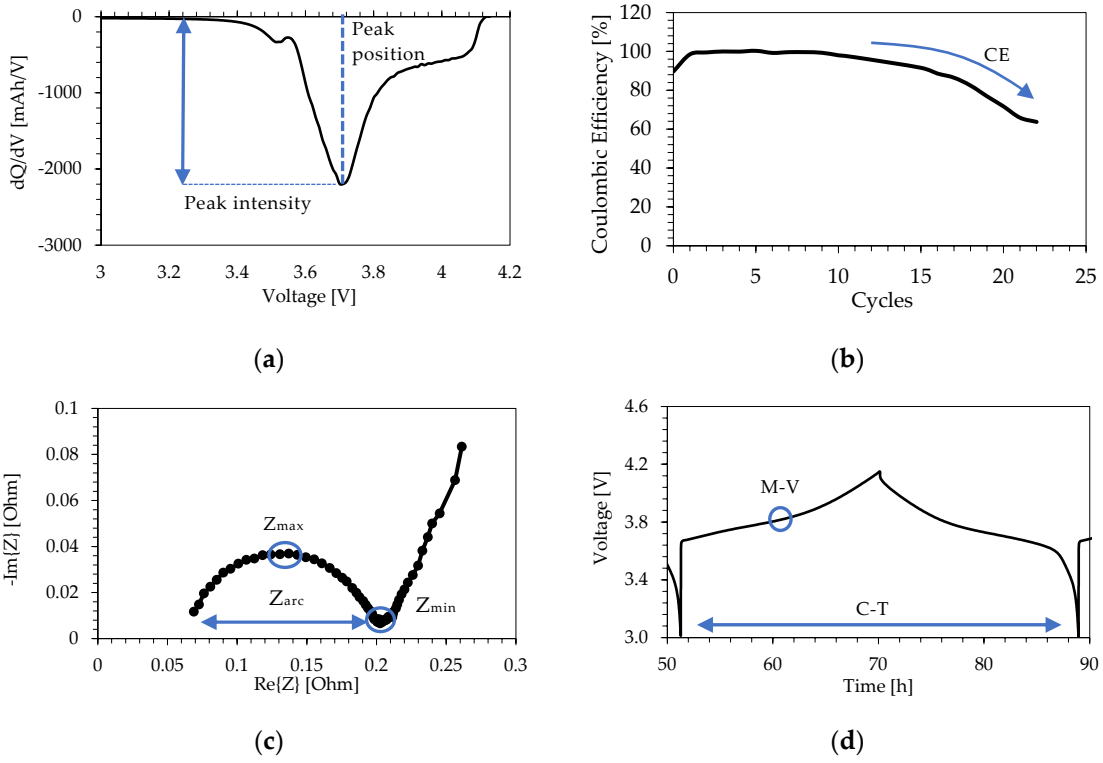

Figure 1. Characterization techniques: (**a**) Incremental Capacity (IC) during discharging phase; (**b**) Coulombic Efficiency (CE); (**c**) EIS spectrum; (**d**) voltage profile with mid-voltage (M-V) and cycle-time (C-T).

Coulombic Efficiency (CE) is a widely used technique exploited to monitor the degradation rate inside a cell [28,33,44–46]. The CE of a cell is defined as the ratio between the delivered capacity during the discharging and during the charging processes of a given cycle; an example of its trend is shown in Figure 1b. In LMBs, the formation of inactive dead lithium leads to a low CE. In [47], C. Fang et al. experimentally demonstrated that the amount of unreacted metallic lithium shows a linear relationship with loss of CE, whereas the lithium ions compound concentration is nearly constant during the CE reduction, implying that the CE decrease in LMB is led by the thickening of the isolated and unreacted lithium layer. Coulombic Efficiency Determination (CED) requires a dedicated test, consisting of continuous cycling at full Depth of Discharge (DoD). In addition, a high sampling rate is required to obtain accurate and reliable CE values, making this technique complicated to be applied and integrated into real BMS systems.

Electrochemical Impedance Spectroscopy (EIS) is a powerful characterization technique consisting of the application of a sinusoidal current signal and measuring the voltage response of the cell at different frequencies to compute the impedance [35,48–53]. Therefore, in BMS applications, a dedicated hardware is required for its application. The resulting impedance curve is normally represented in the Nyquist plot, as shown in Figure 1c and is characterized by three frequency regions [48]: high-frequency region (>1 kHz) including the inductive and ohmic behavior, mid-frequency region (0.1 Hz–1000 Hz) associated to the resistive-capacitive behavior of the charge-transfer processes and low-frequency region (<0.1 Hz) related to the capacitive behavior of the diffusive processes. As observed in [35], EIS spectra throughout cycling are affected by Loss of Lithium Inventory (LLI), that is the consumption of lithium ions by parasitic reaction (SEI growth) and decomposition reactions of the SEI or the electrolyte and LAM processes. EIS has been applied to LMBs [50], showing a large rise of the mid-frequency arch in both real and imaginary impedances and an increase of the ohmic resistance. Impedance evolution during cell aging can be tracked by fitting the curve with Equivalent Circuit Models (ECMs) and by tracking the impedance value of specific parameters (e.g., the maximum of the arch, the width of the arch and the minimum before the tail) [54,55].

Mid-Voltage (M-V) and Cycle-Time (C-T): As a consequence of the dead lithium layer thickening, an increasing electrode overpotential is introduced, leading to an arcing in the voltage profile during the charging process [21]. Furthermore, the increasing overpotential causes the voltage to reach the set maximum and the minimum limit values faster in time during cycling. The evolution of the voltage shape profile (M-V) is recorded by measuring the voltage value at the halfway point in time during charging, as represented in Figure 1d. The time duration of a cycle is then adopted to evaluate the aging state of the cell and the ongoing impact of dead lithium with the C-T parameter.

Table 1 summarizes and ranks the listed characterization techniques depending on different criteria. EIS can be performed in the shortest time. All detection techniques can be implemented into embedded systems (e.g., BMS), but both EIS and CE are considered more complex measurement techniques. IC/DV and EIS parameters allow for the detection of degradation and discriminate the degradation modes (e.g., loss of active material, loss of lithium ions). Mid-Voltage and Cycle Time parameters only allow us to detect the accumulation of dead lithium without more details. Finally, some of the listed techniques allow us to calculate Li plating and stripping rates. These values are useful to quantify the cell degradation in more detail.

2.2. Methodology

The procedure developed to benchmark the detection techniques is schematically represented in Figure 2, including four steps: cell testing, detection parameters identification, thresholds setting and validation. These steps will be described in the next paragraphs.

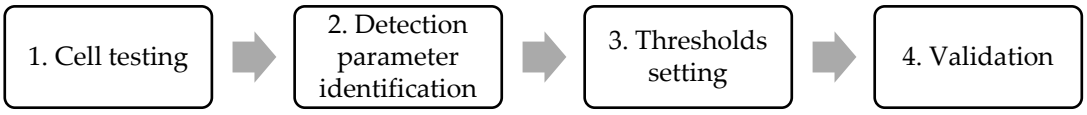

Figure 2. Schematic representation of the developed methodology.

Table 1. Evaluation of measurement and detection characteristics of the techniques analyzed for LMB degradation detection.

Technique	Length	Complexity	Applicability	Degradation Modes	Dendrite Quantification
IC	■■□	■□□	■■□	■■■	■□□
DV	■■□	■□□	■■□	■■■	■■■
CE	■■■	■■□	□□□	■■□	■■■
EIS	■□□	■■□	■■□	■■■	■■□
M–V	■■□	■□□	■■□	■■□	□□□
C–T	■■□	■□□	■■□	■■□	□□□

2.2.1. Cell Testing

A scheme of the cell testing protocol is represented in Figure 3. The procedure is divided in three main steps:

- Formation and characterization: The formation process for the initial SEI layer establishment is performed via two full cycles at low C-rate. The characterization is based on the Battery Capacity Determination (BCD)—a full charge and discharge cycle at specific current rate—and EIS measurements.
- Cycling: consecutive charge–discharge cycles at specific C-rate and DoD.
- Diagnosis: The cell properties are checked regularly after a fixed number of cycles. BCD is performed to obtain the cell's updated capacity (i.e., SoH) and to compute the IC, M-V and C-T characterization techniques. EIS in the frequency range of 10 kHz–10 mHz with C/50 AC current excitation are performed at different OCVs (i.e., SoCs).

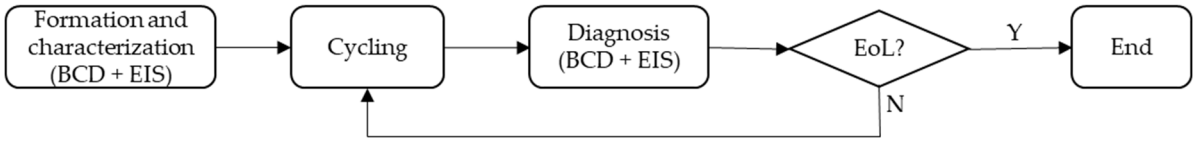

Figure 3. Schematic representation of the cell testing protocol.

After the initial characterization step, cycling and diagnosis are lopped until the cell reaches the End of Life (EoL), represented by a SoH lower than 70%. The only exception is represented by the Coulombic Efficiency protocol, which consists of continuous cycling without interruptions until the EoL of the cell.

2.2.2. Detection Parameters Identification

The experimental results collected during the cell testing are analyzed to define the detection parameters as reported in the last column of Table 2:

- *IC*: The variation of the peak intensity during the discharge phase constitutes a parameter to follow the degradation of the cell. Generally, low current rates during the diagnosis cycle are recommended to have the cell close to equilibrium condition and thus obtain better parameter results. Low rates are preferable (~C/20), but it is proven that even at higher rates (~1C), relevant aging signs are still identifiable [39]. Since the information of the DV and IC profile are similar, only IC analysis is adopted in this study.

- *CE*: The CE technique itself represents the detection parameter.
- *EIS*: Impedance spectra are tracked by recording specific impedance in the three main frequency zones: the local maximum, the width of the mid-frequency semiarch, and the local minimum before the diffusive tail. The resulting Z_{max} Z_{arch}, and Z_{min} represent suitable parameters to track the impedance evolution as the cell faces aging processes. In this study, the imaginary part of Z_{max} and $Z_{min,}$ is used.
- *M-V* and *C-T*: themselves represent the parameters for detection. Both the parameters are retrieved from full diagnosis cycles at regular intervals during testing.

Table 2. Description of characterization techniques and overview of selected detection parameters.

Technique	Measurement Protocol	Elaboration (If Present)	Detection Parameter
IC	Full charge or discharge	$IC = \frac{dQ}{dV}$	Peak intensity
CE	Full cycle	$CE = \frac{Q_{disch}}{Q_{charge}}$	CE value
EIS	EIS	$Z_{arch} = Z_{min} - Z_{ohm}$	Z_{arch}, Z_{max_im}, Z_{min_im}
M–V	Full charge	$Mid - voltage = V_{charge}(t = \frac{t_{charge}}{2})$	M-V
C-T	Full cycle	$Cycle\ time = t_{end} - t_0$	C-T

2.2.3. Thresholds Setting

Through the application of the above presented techniques, the detection parameters are extracted and tracked. Figure 4a exemplifies a parameter variation with respect to its initial value. The parameters usually exhibit small variations between consecutive diagnostic assessments, whereas large and rapid changes occur at later cycles when degradation processes become more relevant. A threshold is set to identify when the transition between the low and high degradation rate occurs:

$$\Delta p = p_i - p_{i-1} > [\text{Threshold}] \quad (1)$$

where Δp is the difference between the actual parameter value p_i and its previous point p_{i-1}. If a threshold is exceeded during testing, as represented at the check n.3 of Figure 4a, a warning signal is triggered to report an upcoming degradation.

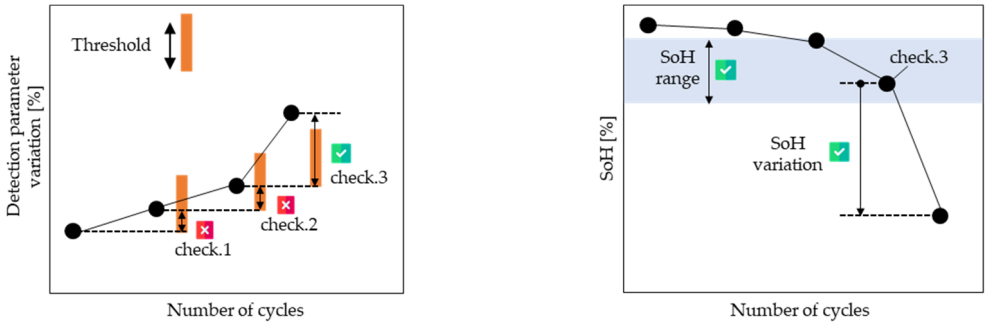

(**a**) (**b**)

Figure 4. Detection algorithm: (**a**) application of thresholds between consecutive measurements of detection parameters; (**b**) validation procedure.

2.2.4. Validation

The validation procedure is then applied to verify whether the warning signal resulting from exceeding a specific parameter threshold truly represents a condition preceding a degradation of the LMB. The process is based on two State of Health (SoH) checks at the triggering event:

- SoH range: At the time when the trigger is activated, the SoH of the cell must be between two limits. This is performed to avoid too early or too late self-healing activation.
- SoH variation: The variation between the SoH of the cell at the time when the trigger is activated and the SoH at the following diagnosis step is used to check if the parameter is detecting and preventing a fast degradation.

Figure 4b shows a graphical representation of the validation procedure for the generic parameter triggered at the check n.3. The fulfillment of both criteria implies that the detection parameter with the selected threshold is suitable for the LMB failure detection.

3. Results and Discussion

Characterization and cycling tests were performed at the Sustainable Energy Center laboratories of CSEM in Neuchâtel, Switzerland with a BioLogic BCS 815 [56] battery tester (±0.01% FSD accuracy on the voltage, ±0.015% FSD accuracy on current, for each available range and EIS capability from 10 kHz to 10 mHz). The cells were placed inside a thermostatic chamber Angelantoni ATT-DM340 [57] to prevent large temperature variations. Table 3 collects the main characteristics of the tests performed on the three batches, under the testing protocol shown in Figure 3: (i) number of cycles performed, the C-rate and voltage range during formation; (ii) capacity determination and EIS during first characterization, (iii) C-rate, DoD and number of cycles applied during cycling phase; and (iv) capacity determination and EIS during the diagnosis phase. In short, the different batches focused on different aspects:

- 1st batch (C-rate focused): The cells are cycled at different C-rates and at full cell capacity (100% DoD), performing a complete diagnosis (BCD+EIS) every 10 cycles.
- 2nd batch (DoD focused): The cells are cycled at reduced DoD, keeping the same C-rate throughout the whole test. EIS during charging are performed every equivalent cycle.
- 3rd batch (hybrid): The tests alternate cycling phases at reduced DoD and full diagnosis every five equivalent cycles.

Table 3. Testing protocol specifications for the three different batches of cells.

	Formation	1st Characterization	Cycling				Diagnosis
			Cell ID	C-Rate	DoD	n. of Cycles	
1st batch	3 cycles, C/10, 3–4.3 V	BCD at C/10, EIS at different SoCs	5	C/10	100%	10	BCD at C/10, EIS at different SoCs
			6	C/5	100%	10	
			7	C/2	100%	10	
			8	1C	100%	10	
			10	C/10	100%	-	CED
			11	C/5	100%	-	CED
			12	C/2	100%	-	CED
2nd batch	2 cycles, C/20, 3–4 V	EIS at 3.8V	15	C/20	20%	5	EIS at 3.8 V
			21	C/20	50%	2	
			22	C/20	80%	1	
			24	C/20	100%	1	
			19	C/10	100%	1	
			17	C/20	100%	-	CED
3rd batch	2 cycles, C/20, 3–4 V	BCD at C/20, EIS at different SoCs	36	C/20	20%	25	BCD at C/10, EIS at different SoCs
			29	C/20	50%	10	
			38	C/20	80%	5	
			37	C/20	100%	5	

The cells that performed Coulombic Efficiency Determination are labelled as "CED" in the column diagnosis (first batch and second batch).

3.1. Testing Results

When analyzing the most relevant results, Figure 5a,b show the SoH evolution retrieved from the BCD diagnosis as a function of the equivalent cycles, respectively, for the 1st and the 3rd batches. EIS spectra evolution (Figure 5c) shows a great rise both in real and imaginary parts as the cell ages. Similarly, the IC profiles (Figure 5d) show a main peak around 3.7 V that consistently decreases its intensity during aging and shifts rightward between the third and fourth diagnosis steps.

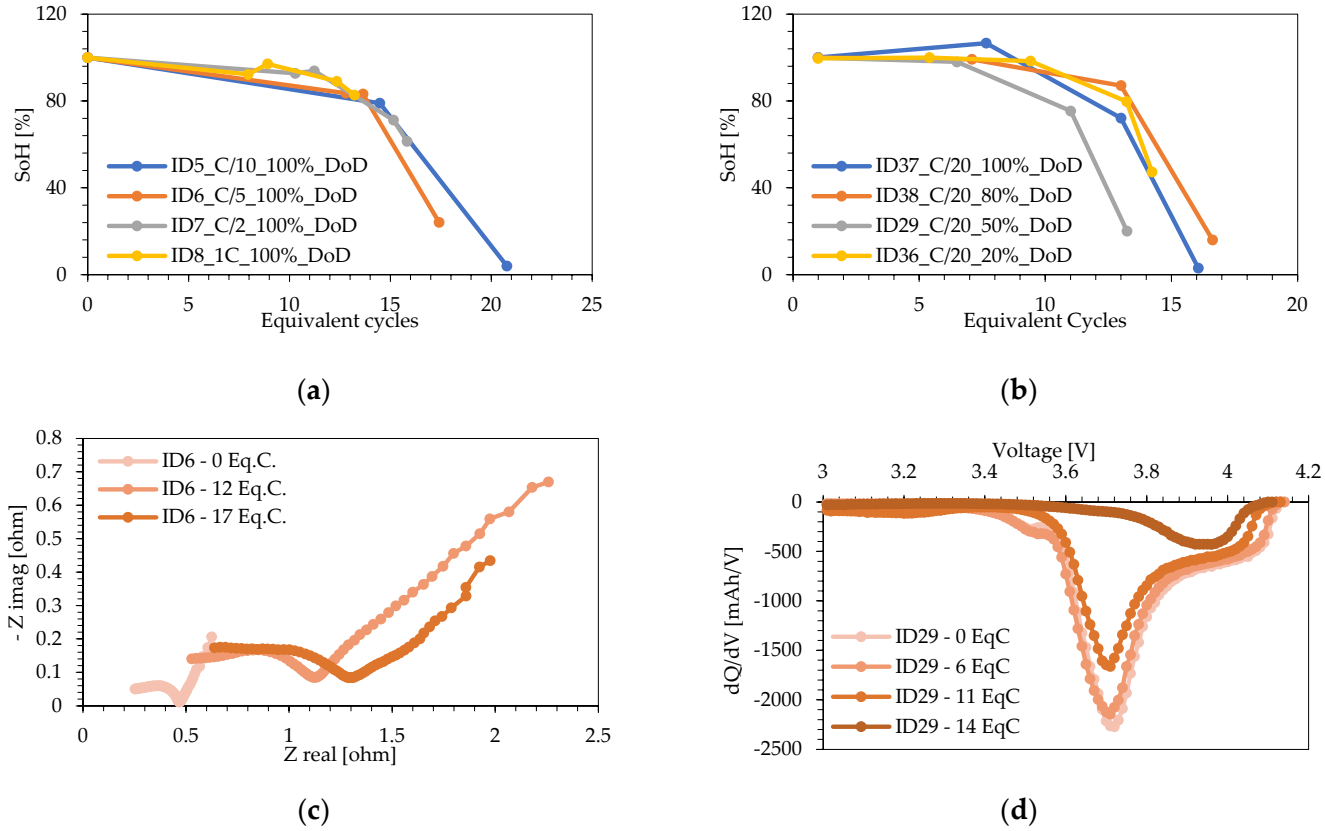

Figure 5. Test results: (**a**) SoH evolution profiles of the 1st batch cells; (**b**) SoH evolution profiles of the 3rd batch cells; (**c**) EIS spectra evolution of cell ID6 at 3.9 V; (**d**) IC profiles of cell ID29.

Figure 6 shows the trends of the detection parameters listed in Table 2 for the 3rd batch cells. For instance, Figure 6a shows the IC peak intensity variation batch, Figure 6b represents the M-V parameter variation and Figure 6c shows the evolution of Z_{arch}. All the parameters are evaluated with respect to their initial value at BoL. The parameters follow a common trend characterized by a sudden increase at the 12th equivalent cycle: this growth is representative of a significant change in cell behavior, and it corresponds to the strong SoH fade represented in Figure 5b.

Lastly, CED is analyzed in Figure 7a,b. The higher the current rate is, the earlier the steep discharge capacity fade occurs, and consequently, the earlier CE drops to values lower than 100%. The irregular trend of cell ID12 suggests that a current rate of C/2 is too high for the cells under investigation.

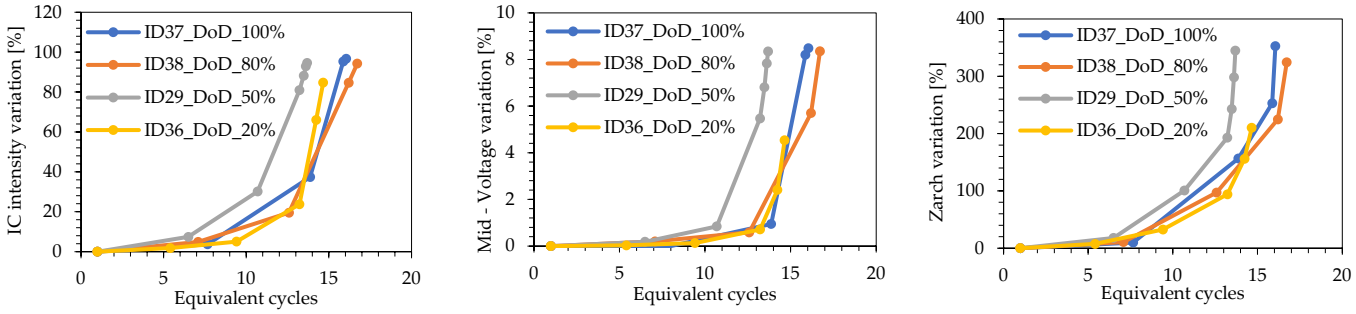

(**a**) (**b**) (**c**)

Figure 6. Examples of detection parameters trends over equivalent cycles for the cells of the 3rd batch: (**a**) IC peak intensity; (**b**) M-V, (**c**) Z_{arch}.

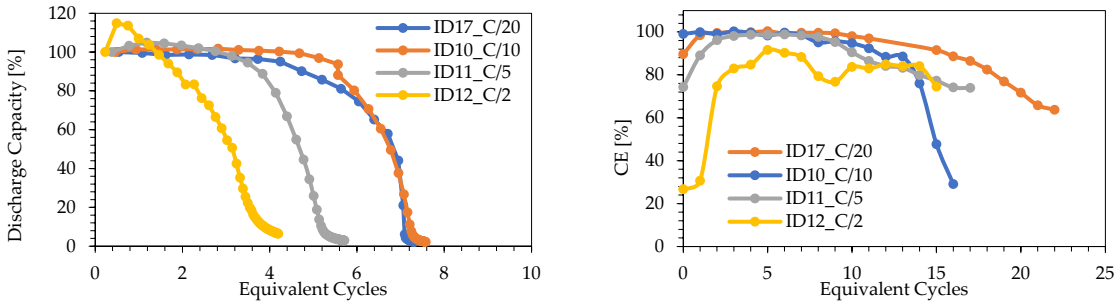

(**a**) (**b**)

Figure 7. CED test results: (**a**) evolution of discharge capacity over equivalent cycles with respect to the initial value; and (**b**) CE trends of the tested cells over the equivalent cycles.

Overall, the collected parameters show clear and distinct signals of cell degradation, i.e., internal physical changes. Given the arcing effect observed in cells voltage profiles during cycling, the degradation is mostly attributed to an accumulation of dead lithium [21]. This phenomenon causes a sudden and steep variation of the detection parameter occurring just after an approximately steady condition.

3.2. Triggering Thresholds and Detection Parameters Validation

As per the procedure detailed in Figure 2, for each of the selected parameters, a suitable threshold has been empirically defined as variation between two consecutive diagnosis steps. Table 4 shows the selected values. In the case of M-V and C-T, a second limit has been introduced to improve reliability of these indicators. The detection techniques with the selected thresholds have been applied to the three batches, with the most representative results reported in Figure 8.

Table 4. Triggering thresholds chosen for the detection parameters investigated.

Parameter	Threshold Values
Mid-Voltage	$(M - V_i) - (M - V_{i-1}) > 1.25\%$ $(M - V_i) - (M - V_0) > 2.5\%$
Cycle Time	$(C - T_i) - (C - T_{i-1}) < 4\%$ $(C - T_i) < 90\%$
Incremental Capacity	$Peak\_Intensity_i – Peak\_intensity_{i-1} > 5\%$
Z_{max_im}	$Z_{max\_i} - Z_{max\_i-1} > 15\%$
Z_{max_im}	$Z_{min\_i} – Z_{min\_i-1} > 15\%$
Z_{arch}	$Z_{arch\_i} - Z_{arch\_i-1} > 15\%$
Coulombic Efficiency	$CE_i - CE_{i-1} > 1.5\%$

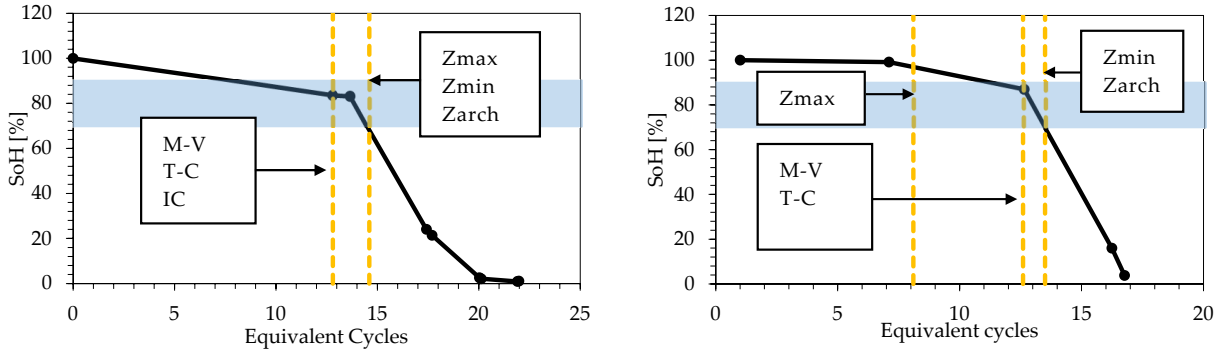

Figure 8. Detection results with triggering highlighted in yellow for: (**a**) cell ID6 of the 1st batch cycling at C/5; (**b**) cell ID38 of the 3rd batch cycling at 80% DoD and C/20.

Regarding the 1st batch experiment, Figure 8a shows that the degradation detection for cell ID6 is triggered in proximity of the SoH slope change for all the tested techniques. Voltage profile-based parameters (i.e., IC, M-V, C-T) showed an earlier detection than impedance-based ones, with the triggering event at the 13th EqC. Similar results were obtained for cell ID38 (third batch), as shown in Figure 8b, with some early triggering by the Z_{max} parameter around the eighth cycle. Analogously, the detection parameters have been evaluated for all the other tested cells. The degradation detection is validated whenever the two criteria presented in Section 2.2.4 are fulfilled, specifically: (i) 70% < SoH_i < 90% and (ii) $SoH_{i+1} - SoH_i \geq 5\%$. Table 5 shows the validation results for the three batches. Unfortunately, the 1st batch has been affected by the limited number of diagnostic phases in the tests. In the case of the 2nd and 3rd batches, M-V, C-T and IC peak intensity parameters fulfill both validation criteria in almost all the testing conditions suggesting a good performance of the parameters to detect degradation.

Table 5. Validation procedure results for the three batch tests. The columns correspond to the testing conditions and the rows to the detection parameters. The legend is given in the lower part of the table.

Parameter	**1st Batch**					**2nd Batch**					**3rd Batch**			
	C/10—100% DoD	C/5—100% DoD	C/2—100% DoD	1C—100% DoD	C/20—100% DoD	C/10—100% DoD	C/20—80% DoD	C/20—50% DoD	C/20—20% DoD	C/20—100% DoD	C/20—80% DoD	C/20—50% DoD	C/20—20% DoD
Z_{max_im}	√|√	√|√	×|×	×|×	×|×	√|√	√|√	√|√	×|√	√|×	×|×	×|×	×|×
Z_{min_im}	√|√	√|√	×|×	×|×	√|√	√|√	√|√	√|√	√|×	√|×	√|√	×|√	×|√
Z_{arch}	√|√	√|√	×|×	×|×	√|√	√|√	√|√	√|√	×|√	√|×	√|√	×|×	×|×
M-V	√|√	√|√	×|×	×|×	×|×	×|√	√|√	×|√	√|×	√|√	√|√	√|√	√|√
C-T	√|√	√|√	×|×	√|√	√|×	√|√	×|√	√|√	√|×	√|√	√|√	√|√	√|√
IC peak intensity	√|√	√|√	×|×	×|×	×|×	√|√	×|√	√|√	√|√	√|√	√|√	×|×	√|√
CE	×|√	√|√	√|√	–	√|√	–	–	–	–	–	–	–	–
Legend	×|×: both SoH checks failed							√|×: SoH range fulfilled; SoH variation failed					
	√|√: both SoH checks fulfilled							×|√: SoH range failed; SoH variation fulfilled					

3.3. Sensitivity Analysis

A sensitivity analysis was applied to identify the best values for the parameters' thresholds (Table 6). Ten different thresholds values were tested for each detection parameter. The

sensitivity analysis was applied only to the 2nd and 3rd batches, given the few diagnosis points available in the 1st batch. The thresholds are evaluated separately, and the detection Success Rate was computed, i.e., the ratio between the number of cases where the SoH validation criterium was fulfilled over the total number of tested cases.

Table 6. Success rate results for SoH range and SoH variation validation procedures with the parameter thresholds selected for the sensitivity analysis application.

Z_{max_im} [%]	**Thresholds**	**2.5%**	**5%**	**7.5%**	**10%**	**12.5%**	**15%**	**17.5%**	**20%**	**22.5%**	**25%**
	SoH range	22%	22%	22%	33%	33%	33%	22%	44%	22%	22%
	SoH var.	44%	44%	56%	56%	56%	56%	56%	78%	67%	78%
Z_{min_im} [%]	**Thresholds**	**2.5%**	**5%**	**7.5%**	**10%**	**12.5%**	**15%**	**17.5%**	**20%**	**22.5%**	**25%**
	SoH range	22%	22%	22%	44%	56%	67%	67%	67%	56%	33%
	SoH var.	44%	44%	44%	67%	78%	89%	89%	89%	100%	78%
Z_{arch} [%]	**Thresholds**	**2.5%**	**5%**	**7.5%**	**10%**	**12.5%**	**15%**	**17.5%**	**20%**	**22.5%**	**25%**
	SoH range	22%	33%	33%	33%	44%	44%	44%	56%	33%	22%
	SoH var.	44%	44%	44%	56%	67%	67%	67%	89%	78%	67%
M-V [%]	**Thresholds**	**0.1%**	**0.25%**	**0.5%**	**0.75%**	**1%**	**1.25%**	**1.5%**	**2%**	**2.25%**	**2.5%**
	SoH range	33%	33%	44%	67%	67%	67%	56%	44%	44%	44%
	SoH var.	44%	44%	56%	78%	78%	78%	67%	78%	67%	67%
C-T [%]	**Thresholds**	**1%**	**1.5%**	**2%**	**2.5%**	**3%**	**4%**	**5%**	**6%**	**7.5%**	**10%**
	SoH range	33%	44%	56%	56%	78%	89%	100%	100%	100%	100%
	SoH var.	56%	56%	67%	67%	78%	78%	78%	78%	78%	78%
IC [%]	**Thresholds**	**0.25%**	**0.5%**	**0.75%**	**1%**	**2.5%**	**5%**	**7.5%**	**10%**	**12.5%**	**15%**
	SoH range	11%	11%	11%	11%	22%	56%	67%	67%	67%	56%
	SoH var.	44%	44%	44%	44%	44%	78%	89%	100%	89%	67%
CE [%]	**Thresholds**	**0.1%**	**0.25%**	**0.5%**	**1%**	**1.5%**	**2%**	**2.5%**	**3%**	**4%**	**5%**
	SoH range	25%	25%	25%	50%	50%	50%	50%	50%	50%	25%
	SoH var.	0%	0%	25%	25%	75%	50%	50%	50%	75%	50%

The resulting Success Rates are reported in Table 6, respectively, for the SoH range and the SoH variation validation criteria. In the first case, mid-range thresholds allow for a higher success rate applying all the detection techniques. Too small or too high threshold values are ineffective, respectively, with too early and too late detection. In the second case, the results for the SoH variation are very similar, even though larger threshold values give a higher success rate for most of the techniques.

Thresholds' Success Rates for the two validation criteria were then combined by retaining the lowest Success Rate value among the two applied criteria. The best threshold value is defined as the one with the highest success rate for a specific detection parameter. The results are listed in Table 7. Overall, the Cycle Time obtained the highest success rate of 78%, the Mid-Voltage and IC peak intensity share the same success rate of 67%, whereas the best performing impedance-based parameter is Z_{min} with a 67% success rate, followed by Z_{arch} and finally Z_{max}. Lastly, the CE parameter led to effective detection in only half of the tested cases.

Table 7. Sensitivity analysis results.

Parameter	Threshold Value [%]	Success Rate [%]
Z_{max_im}	20%	44%
Z_{min_im}	15%	67%
Z_{arch_im}	20%	56%
M-V	0.75%	67%
C-T	3%	78%
IC	7.5%	67%
CE	1.5%	50%

4. Conclusions

This work introduced a structured methodology to test and validate parameters that can be used to detect degradation in LMB and which should be non-invasive and BMS-triggerable. In this way, a novel algorithm structure is presented to enable LMB degradation tracking and to trigger self-healing mechanism activation by BMS. After a review of the selected electrochemical techniques (Section 1), Section 2 presented the developed methodology which includes (i) the cycling and diagnosis of standard LMBs via six testing protocols, (ii) the analysis on the selected detection parameters trends with respect to capacity fade, (iii) the thresholds definition to trigger a self-healing action and (iv) the performance validation in early detecting LMBs degradation. Section 3 presented the case study where three batches of LMBs have been tested with different protocol focus: different C-rates and 100% DoD, fixed C-rate and different DoD ranges. A sensitivity analysis was performed to compute the Success Rate of each detection technique. On average, the detection techniques successfully detected degradation in 60% of the cases and can be used to anticipate LMB failures and to lay the basis for self-healing mechanism activation.

Limitations of this work can be analyzed on different levels. *Validity of the results*: The obtained Success Rate was not directly linked to the ability to detect dendrite growth formation. During the experimental phase, it was in fact not possible to discriminate dendrite growth from dead lithium, the fast accumulation of which was confirmed by post-mortem analysis. All the tested cells reached their EoL due to cycling failure and not for short-circuit failure. *Replicability of the results*: The obtained Success Rates are very dependent on the experimental campaign performed for two reasons: statistics, due to the limited number of tested samples, and specificities of the tested cells (Li||NMC). The developed methodology can be replicated to other LMB with different chemical formulation, but different performance results should be expected. These results could also be influenced by more severe or real use profiles testing conditions. *Applicability of the results*: The tested detection techniques can be implemented in embedded systems to sense degradation and trigger actions such as, for instance, self-healing methods, which is one of the possible routes to make LMB exploitable in real applications. Some techniques are easier than others, but in general all the non-invasive techniques proposed can be implemented in BMSs.

Author Contributions: Conceptualization, P.I. and C.B.; methodology, L.L. and P.I.; validation, L.L.; investigation, L.L. and P.I.; writing—original draft preparation, L.L.; writing—review and editing, P.I. and C.B.; visualization, P.I.; supervision, C.B.; funding acquisition, C.B. All authors have read and agreed to the published version of the manuscript.

Funding: This research was funded by the HIDDEN project that receives funding from the European Union's Horizon 2020 research and innovation programme under Grant Agreement No. 957202.

Data Availability Statement: The data presented in this study are openly available in Zenodo at 10.5281/zenodo.7007544.

Acknowledgments: The authors would like to thank Marco Merlo, Energy Department, Politecnico di Milano, Milano (Italy) for his support in developing the testing methodology.

Conflicts of Interest: The authors declare no conflict of interest.

References

1. Tian, Y.; Zeng, G.; Rutt, A.; Shi, T.; Kim, H.; Wang, J.; Koettgen, J.; Sun, Y.; Ouyang, B.; Chen, T.; et al. Promises and Challenges of Next-Generation "Beyond Li-Ion" Batteries for Electric Vehicles and Grid Decarbonization. *Chem. Rev.* **2021**, *121*, 1623–1669. [CrossRef]
2. Shen, X.; Liu, H.; Cheng, X.-B.; Yan, C.; Huang, J.-Q. Beyond Lithium Ion Batteries: Higher Energy Density Battery Systems Based on Lithium Metal Anodes. *Energy Storage Mater.* **2018**, *12*, 161–175. [CrossRef]
3. Thackeray, M.M.; Wolverton, C.; Isaacs, E.D. Electrical Energy Storage for Transportation—Approaching the Limits of, and Going beyond, Lithium-Ion Batteries. *Energy Environ. Sci.* **2012**, *5*, 7854. [CrossRef]
4. Divakaran, A.M.; Minakshi, M.; Bahri, P.A.; Paul, S.; Kumari, P.; Divakaran, A.M.; Manjunatha, K.N. Rational Design on Materials for Developing next Generation Lithium-Ion Secondary Battery. *Prog. Solid State Chem.* **2021**, *62*, 100298. [CrossRef]
5. Wang, R.; Cui, W.; Chu, F.; Wu, F. Lithium Metal Anodes: Present and Future. *J. Energy Chem.* **2020**, *48*, 145–159. [CrossRef]
6. Wang, Z.; Cao, Y.; Zhou, J.; Liu, J.; Shen, X.; Ji, H.; Yan, C.; Qian, T. Processing Robust Lithium Metal Anode for High-Security Batteries: A Minireview. *Energy Storage Mater.* **2022**, *47*, 122–133. [CrossRef]
7. Aurbach, D. A Short Review of Failure Mechanisms of Lithium Metal and Lithiated Graphite Anodes in Liquid Electrolyte Solutions. *Solid State Ion.* **2002**, *148*, 405–416. [CrossRef]
8. Lu, D.; Shao, Y.; Lozano, T.; Bennett, W.D.; Graff, G.L.; Polzin, B.; Zhang, J.; Engelhard, M.H.; Saenz, N.T.; Henderson, W.A.; et al. Failure Mechanism for Fast-Charged Lithium Metal Batteries with Liquid Electrolytes. *Adv. Energy Mater.* **2015**, *5*, 1400993. [CrossRef]
9. Zhang, Y.; Zhong, Y.; Shi, Q.; Liang, S.; Wang, H. Cycling and Failing of Lithium Metal Anodes in Carbonate Electrolyte. *J. Phys. Chem. C* **2018**, *122*, 21462–21467. [CrossRef]
10. Raj, V.; Aetukuri, N.P.B.; Nanda, J. Solid State Lithium Metal Batteries—Issues and Challenges at the Lithium-Solid Electrolyte Interface. *Curr. Opin. Solid State Mater. Sci.* **2022**, *26*, 100999. [CrossRef]
11. Wood, K.N.; Noked, M.; Dasgupta, N.P. Lithium Metal Anodes: Toward an Improved Understanding of Coupled Morphological, Electrochemical, and Mechanical Behavior. *ACS Energy Lett.* **2017**, *2*, 664–672. [CrossRef]
12. Wood, K.N.; Kazyak, E.; Chadwick, A.F.; Chen, K.-H.; Zhang, J.-G.; Thornton, K.; Dasgupta, N.P. Dendrites and Pits: Untangling the Complex Behavior of Lithium Metal Anodes through Operando Video Microscopy. *ACS Cent. Sci.* **2016**, *2*, 790–801. [CrossRef]
13. Stark, J.K.; Ding, Y.; Kohl, P.A. Nucleation of Electrodeposited Lithium Metal: Dendritic Growth and the Effect of Co-Deposited Sodium. *J. Electrochem. Soc.* **2013**, *160*, D337–D342. [CrossRef]
14. Horstmann, B.; Shi, J.; Amine, R.; Werres, M.; He, X.; Jia, H.; Hausen, F.; Cekic-Laskovic, I.; Wiemers-Meyer, S.; Lopez, J.; et al. Strategies towards Enabling Lithium Metal in Batteries: Interphases and Electrodes. *Energy Environ. Sci.* **2021**, *14*, 5289–5314. [CrossRef]
15. Frenck, L.; Sethi, G.K.; Maslyn, J.A.; Balsara, N.P. Factors That Control the Formation of Dendrites and Other Morphologies on Lithium Metal Anodes. *Front. Energy Res.* **2019**, *7*, 115. [CrossRef]
16. Bai, P.; Li, J.; Brushett, F.R.; Bazant, M.Z. Transition of Lithium Growth Mechanisms in Liquid Electrolytes. *Energy Environ. Sci.* **2016**, *9*, 3221–3229. [CrossRef]
17. Kong, L.; Xing, Y.; Pecht, M.G. In-Situ Observations of Lithium Dendrite Growth. *IEEE Access* **2018**, *6*, 8387–8393. [CrossRef]
18. Rosso, M.; Brissot, C.; Teyssot, A.; Dollé, M.; Sannier, L.; Tarascon, J.-M.; Bouchet, R.; Lascaud, S. Dendrite Short-Circuit and Fuse Effect on Li/Polymer/Li Cells. *Electrochim. Acta* **2006**, *51*, 5334–5340. [CrossRef]
19. Xu, S.; Chen, K.-H.; Dasgupta, N.P.; Siegel, J.B.; Stefanopoulou, A.G. Evolution of Dead Lithium Growth in Lithium Metal Batteries: Experimentally Validated Model of the Apparent Capacity Loss. *J. Electrochem. Soc.* **2019**, *166*, A3456–A3463. [CrossRef]
20. Aryanfar, A.; Brooks, D.J.; Colussi, A.J.; Hoffmann, M.R. Quantifying the Dependence of Dead Lithium Losses on the Cycling Period in Lithium Metal Batteries. *Phys. Chem. Chem. Phys.* **2014**, *16*, 24965–24970. [CrossRef]
21. Chen, K.-H.; Wood, K.N.; Kazyak, E.; LePage, W.S.; Davis, A.L.; Sanchez, A.J.; Dasgupta, N.P. Dead Lithium: Mass Transport Effects on Voltage, Capacity, and Failure of Lithium Metal Anodes. *J. Mater. Chem. A* **2017**, *5*, 11671–11681. [CrossRef]
22. Niu, C.; Lee, H.; Chen, S.; Li, Q.; Du, J.; Xu, W.; Zhang, J.-G.; Whittingham, M.S.; Xiao, J.; Liu, J. High-Energy Lithium Metal Pouch Cells with Limited Anode Swelling and Long Stable Cycles. *Nat. Energy* **2019**, *4*, 551–559. [CrossRef]
23. Narayan, R.; Laberty-Robert, C.; Pelta, J.; Tarascon, J.-M.; Dominko, R. Self-Healing: An Emerging Technology for Next-Generation Smart Batteries. *Adv. Energy Mater.* **2022**, *12*, 2102652. [CrossRef]
24. Hu, Z.; Li, G.; Wang, A.; Luo, J.; Liu, X. Recent Progress of Electrolyte Design for Lithium Metal Batteries. *Batter. Supercaps* **2020**, *3*, 331–335. [CrossRef]
25. Ma, L.; Cui, J.; Yao, S.; Liu, X.; Luo, Y.; Shen, X.; Kim, J.-K. Dendrite-Free Lithium Metal and Sodium Metal Batteries. *Energy Storage Mater.* **2020**, *27*, 522–554. [CrossRef]
26. Gao, T.; Rainey, C.; Lu, W. Piezoelectric Mechanism and a Compliant Film to Effectively Suppress Dendrite Growth. *ACS Appl. Mater. Interfaces* **2020**, *12*, 51448–51458. [CrossRef]
27. Liu, G.; Wang, D.; Zhang, J.; Kim, A.; Lu, W. Preventing Dendrite Growth by a Soft Piezoelectric Material. *ACS Mater. Lett.* **2019**, *1*, 498–505. [CrossRef]
28. Paul, P.P.; McShane, E.J.; Colclasure, A.M.; Balsara, N.; Brown, D.E.; Cao, C.; Chen, B.; Chinnam, P.R.; Cui, Y.; Dufek, E.J.; et al. A Review of Existing and Emerging Methods for Lithium Detection and Characterization in Li-Ion and Li-Metal Batteries. *Adv. Energy Mater.* **2021**, *11*, 2100372. [CrossRef]

29. Konz, Z.M.; McShane, E.J.; McCloskey, B.D. Detecting the Onset of Lithium Plating and Monitoring Fast Charging Performance with Voltage Relaxation. *ACS Energy Lett.* **2020**, *5*, 1750–1757. [CrossRef]
30. Attia, P.M.; Grover, A.; Jin, N.; Severson, K.A.; Markov, T.M.; Liao, Y.-H.; Chen, M.H.; Cheong, B.; Perkins, N.; Yang, Z.; et al. Closed-Loop Optimization of Fast-Charging Protocols for Batteries with Machine Learning. *Nature* **2020**, *578*, 397–402. [CrossRef]
31. The HIDDEN Project. Available online: https://hidden-project.eu/ (accessed on 21 March 2022).
32. Berecibar, M.; Dubarry, M.; Omar, N.; Villarreal, I.; Van Mierlo, J. Degradation Mechanism Detection for NMC Batteries Based on Incremental Capacity Curves. *World Electr. Veh. J.* **2016**, *8*, 350–361. [CrossRef]
33. Yang, F.; Wang, D.; Zhao, Y.; Tsui, K.-L.; Bae, S.J. A Study of the Relationship between Coulombic Efficiency and Capacity Degradation of Commercial Lithium-Ion Batteries. *Energy* **2018**, *145*, 486–495. [CrossRef]
34. Li, X.; Yuan, C.; Li, X.; Wang, Z. State of Health Estimation for Li-Ion Battery Using Incremental Capacity Analysis and Gaussian Process Regression. *Energy* **2020**, *190*, 116467. [CrossRef]
35. Pastor-Fernández, C.; Uddin, K.; Chouchelamane, G.H.; Widanage, W.D.; Marco, J. A Comparison between Electrochemical Impedance Spectroscopy and Incremental Capacity-Differential Voltage as Li-Ion Diagnostic Techniques to Identify and Quantify the Effects of Degradation Modes within Battery Management Systems. *J. Power Sources* **2017**, *360*, 301–318. [CrossRef]
36. Krupp, A.; Ferg, E.; Schuldt, F.; Derendorf, K.; Agert, C. Incremental Capacity Analysis as a State of Health Estimation Method for Lithium-Ion Battery Modules with Series-Connected Cells. *Batteries* **2020**, *7*, 2. [CrossRef]
37. Dubarry, M.; Svoboda, V.; Hwu, R.; Liaw, B.Y. Incremental Capacity Analysis and Close-to-Equilibrium OCV Measurements to Quantify Capacity Fade in Commercial Rechargeable Lithium Batteries. *Electrochem. Solid-State Lett.* **2006**, *9*, A454. [CrossRef]
38. Anseán, D.; García, V.M.; González, M.; Blanco-Viejo, C.; Viera, J.C.; Pulido, Y.F.; Sánchez, L. Lithium-Ion Battery Degradation Indicators Via Incremental Capacity Analysis. *IEEE Trans. Ind. Appl.* **2019**, *55*, 2992–3002. [CrossRef]
39. Plattard, T.; Barnel, N.; Assaud, L.; Franger, S.; Duffault, J.-M. Combining a Fatigue Model and an Incremental Capacity Analysis on a Commercial NMC/Graphite Cell under Constant Current Cycling with and without Calendar Aging. *Batteries* **2019**, *5*, 36. [CrossRef]
40. Schmitt, J.; Schindler, M.; Oberbauer, A.; Jossen, A. Determination of Degradation Modes of Lithium-Ion Batteries Considering Aging-Induced Changes in the Half-Cell Open-Circuit Potential Curve of Silicon–Graphite. *J. Power Source* **2022**, *532*, 231296. [CrossRef]
41. Kato, H.; Kobayashi, Y.; Miyashiro, H. Differential Voltage Curve Analysis of a Lithium-Ion Battery during Discharge. *J. Power Source* **2018**, *398*, 49–54. [CrossRef]
42. Bloom, I.; Walker, L.K.; Basco, J.K.; Abraham, D.P.; Christophersen, J.P.; Ho, C.D. Differential Voltage Analyses of High-Power Lithium-Ion Cells. 4. Cells Containing NMC. *J. Power Source* **2010**, *195*, 877–882. [CrossRef]
43. Keil, P.; Jossen, A. Calendar Aging of NCA Lithium-Ion Batteries Investigated by Differential Voltage Analysis and Coulomb Tracking. *J. Electrochem. Soc.* **2017**, *164*, A6066. [CrossRef]
44. Xiao, J.; Li, Q.; Bi, Y.; Cai, M.; Dunn, B.; Glossmann, T.; Liu, J.; Osaka, T.; Sugiura, R.; Wu, B.; et al. Understanding and Applying Coulombic Efficiency in Lithium Metal Batteries. *Nat. Energy* **2020**, *5*, 561–568. [CrossRef]
45. Burns, J.C.; Stevens, D.A.; Dahn, J.R. In-Situ Detection of Lithium Plating Using High Precision Coulometry. *J. Electrochem. Soc.* **2015**, *162*, A959–A964. [CrossRef]
46. Adams, B.D.; Zheng, J.; Ren, X.; Xu, W.; Zhang, J.-G. Accurate Determination of Coulombic Efficiency for Lithium Metal Anodes and Lithium Metal Batteries. *Adv. Energy Mater.* **2018**, *8*, 1702097. [CrossRef]
47. Fang, C.; Li, J.; Zhang, M.; Zhang, Y.; Yang, F.; Lee, J.Z.; Lee, M.-H.; Alvarado, J.; Schroeder, M.A.; Yang, Y.; et al. Quantifying Inactive Lithium in Lithium Metal Batteries. *Nature* **2019**, *572*, 511–515. [CrossRef]
48. Iurilli, P.; Brivio, C.; Wood, V. On the Use of Electrochemical Impedance Spectroscopy to Characterize and Model the Aging Phenomena of Lithium-Ion Batteries: A Critical Review. *J. Power Source* **2021**, *505*, 229860. [CrossRef]
49. Westerhoff, U.; Kurbach, K.; Lienesch, F.; Kurrat, M. Analysis of Lithium-Ion Battery Models Based on Electrochemical Impedance Spectroscopy. *Energy Technol.* **2016**, *4*, 1620–1630. [CrossRef]
50. Bieker, G.; Winter, M.; Bieker, P. Electrochemical in Situ Investigations of SEI and Dendrite Formation on the Lithium Metal Anode. *Phys. Chem. Chem. Phys.* **2015**, *17*, 8670–8679. [CrossRef]
51. Tröltzsch, U.; Kanoun, O.; Tränkler, H.-R. Characterizing Aging Effects of Lithium Ion Batteries by Impedance Spectroscopy. *Electrochim. Acta* **2005**, *51*, 1664–1672. [CrossRef]
52. Zhang, Q.; Wang, D.; Schaltz, E.; Stroe, D.-I.; Gismero, A.; Yang, B. Degradation Mechanism Analysis and State-of-Health Estimation for Lithium-Ion Batteries Based on Distribution of Relaxation Times. *J. Energy Storage* **2022**, *55*, 105386. [CrossRef]
53. Iurilli, P.; Brivio, C.; Wood, V. Detection of Lithium-Ion Cells' Degradation through Deconvolution of Electrochemical Impedance Spectroscopy with Distribution of Relaxation Time. *Energy Technol.* **2022**, 2200547. [CrossRef]
54. Estaller, J.; Kersten, A.; Kuder, M.; Thiringer, T.; Eckerle, R.; Weyh, T. Overview of Battery Impedance Modeling Including Detailed State-of-the-Art Cylindrical 18650 Lithium-Ion Battery Cell Comparisons. *Energies* **2022**, *15*, 3822. [CrossRef]
55. Uddin, K.; Perera, S.; Widanage, W.D.; Somerville, L.; Marco, J. Characterising Lithium-Ion Battery Degradation through the Identification and Tracking of Electrochemical Battery Model Parameters. *Batteries* **2016**, *2*, 13. [CrossRef]
56. Product Specifications—Battery Tester BCS-800 Series. Available online: https://www.biologic.net/documents/hight-throughput-battery-tester-bcs-8xx-series/ (accessed on 16 April 2021).
57. Angelantoni Test Technologies Discovery Climatic Chambers. Available online: https://www.acstestchambers.com/en/environmental-test-chambers/discovery-my-climatic-chambers-for-stress-screening/ (accessed on 16 April 2021).